



Neon diffusion kinetics and implications for cosmogenic neon paleothermometry in feldspars

Marissa M. Tremblay^{a,b,*}, David L. Shuster^{a,b}, Greg Balco^b, William S. Cassata^c

^a Department of Earth and Planetary Science, University of California, Berkeley, 307 McCone Hall #4767, Berkeley, CA 94720-4767, USA

^b Berkeley Geochronology Center, 2455 Ridge Road, Berkeley, CA 94709, USA

^c Chemical Sciences Division, Lawrence Livermore National Laboratory, 7000 East Avenue (L-231), Livermore, CA 94550, USA

Received 27 August 2016; accepted in revised form 10 February 2017; Available online 20 February 2017

Abstract

Observations of cosmogenic neon concentrations in feldspars can potentially be used to constrain the surface exposure duration or surface temperature history of geologic samples. The applicability of cosmogenic neon to either application depends on the temperature-dependent diffusivity of neon isotopes. In this work, we investigate the kinetics of neon diffusion in feldspars of different compositions and geologic origins through stepwise degassing experiments on single, proton-irradiated crystals. To understand the potential causes of complex diffusion behavior that is sometimes manifest as nonlinearity in Arrhenius plots, we compare our results to argon stepwise degassing experiments previously conducted on the same feldspars. Many of the feldspars we studied exhibit linear Arrhenius behavior for neon whereas argon degassing from the same feldspars did not. This suggests that nonlinear behavior in argon experiments is an artifact of structural changes during laboratory heating. However, other feldspars that we examined exhibit nonlinear Arrhenius behavior for neon diffusion at temperatures far below any known structural changes, which suggests that some preexisting material property is responsible for the complex behavior. In general, neon diffusion kinetics vary widely across the different feldspars studied, with estimated activation energies (E_a) ranging from 83.3 to 110.7 kJ/mol and apparent pre-exponential factors (D_0) spanning three orders of magnitude from 2.4×10^{-3} to $8.9 \times 10^{-1} \text{ cm}^2 \text{ s}^{-1}$. As a consequence of this variability, the ability to reconstruct temperatures or exposure durations from cosmogenic neon abundances will depend on both the specific feldspar and the surface temperature conditions at the geologic site of interest.

© 2017 Elsevier Ltd. All rights reserved.

Keywords: Cosmogenic nuclide; Noble gas; Diffusion; Thermochronometry; Paleoclimate; Surface processes

1. INTRODUCTION

In noble gas thermochronometry, the thermal histories of geologic materials are inferred from the concurrent production and thermally-activated diffusion of noble gases.

* Corresponding author at: Department of Earth and Planetary Science, University of California, Berkeley, 307 McCone Hall #4767, Berkeley, CA 94720-4767, USA.

E-mail addresses: mtremblay@berkeley.edu (M.M. Tremblay), dshuster@berkeley.edu (D.L. Shuster), balcs@bgc.org (G. Balco), cassata2@llnl.gov (W.S. Cassata).

These thermal histories can be used to understand geologic processes occurring over a vast range of temperatures and timescales, from erosion-driven exhumation of rocks over millions of years (e.g., [Herman et al., 2013](#), and references therein) to near instantaneous high-temperature impact events (e.g., [Min et al., 2004](#); [Cassata et al., 2010](#); [Jourdan et al., 2011](#)). Feldspar minerals are frequently utilized for noble gas thermochronometry because they are abundant in silicic rocks and have compositions that permit high noble gas production rates from both radioactive decay (radiogenic noble gases) and *in situ* nuclear interactions with secondary cosmic-ray particles (cosmogenic

noble gases). Since its development nearly half a century ago, feldspar $^{40}\text{Ar}/^{39}\text{Ar}$ thermochronometry, which utilizes the production and diffusion of radiogenic ^{40}Ar , has been extensively used to study crustal and surface processes both on Earth (e.g., Richter et al., 1991; Hodges et al., 2005) and other planetary bodies (e.g., Turner, 1971; Shuster et al., 2010). More recently, cosmogenic argon in feldspars has been used to reconstruct planetary surface temperatures (e.g., Shuster and Cassata, 2015). Cosmogenic neon in feldspars can, in theory, also be used for surface temperature thermochronometry (Tremblay et al., 2014a; Garrick-Bethell et al., 2017). If neon is quantitatively retained in feldspars at planetary surface temperatures, cosmogenic neon measurements can also be used to determine surface exposure durations (e.g., Kober et al., 2005).

The production and diffusion systematics of a particular noble gas–mineral pair must be known for thermochronometric or geochronologic applications. Here, we focus on empirical quantification of neon diffusion kinetics in feldspars, with the goal of examining whether cosmogenic neon can be used for surface paleothermometry (Tremblay et al., 2014a). The only existing constraints on neon diffusion in feldspars were reported by Gourbet et al. (2012), who examined the diffusion kinetics of neutron-induced ^{22}Ne in three alkali feldspars through stepwise degassing experiments. Orthoclase and Ca-rich anorthoclase exhibited relatively simple neon diffusion behavior expressed as a linear relationship between the logarithm of diffusivity and inverse temperature (although the linearity of the orthoclase experiment has been questioned (Lovera et al., 2015)), while Fish Canyon Tuff sanidine did not. The range in Arrhenius diffusion parameters (activation energy, E_a , and pre-exponential factor, D_0) calculated by Gourbet et al. (2012) suggest that neon can be quantitatively retained at Earth surface temperatures over millions of years, in the case of the orthoclase studied, or diffusively lost on thousand year timescales, in the case of anorthoclase and sanidine.

Several questions remain from these initial experiments reported by Gourbet et al. (2012) that we aim to address. First, what is the kinetics of neon diffusion in plagioclase feldspars? Gourbet et al. (2012) studied three alkali feldspars; no experimental work has quantified the kinetics of neon diffusion in plagioclases. To fill this gap, we present results from stepwise degassing experiments on three plagioclase feldspars. We also discuss results from a stepwise degassing experiment on an endmember plagioclase feldspar from lunar sample 76535 (Garrick-Bethell et al., 2017).

Second, how do the kinetics and behaviors of neon and argon diffusion compare? In contrast to neon, there is a vast literature exploring the kinetics of argon diffusion in feldspars. Some of the earliest studies examining argon in geologic materials (e.g., Reynolds, 1957; Fechtig et al., 1960; Evernden et al., 1960; Gerling et al., 1963) found evidence for complex diffusion behavior in feldspars, which has been observed numerous times since (e.g. Lovera et al., 1997, and references therein; Berger and York, 1981; Harrison and McDougall, 1982; Cassata and Renne, 2013). The origin and significance of complex argon diffusion behavior, which is observed as both nonlinear Arrhenius arrays and age spectra with multiple plateaus, has been discussed at length.

Multiple diffusion domain (MDD) theory (Lovera and Richter, 1989; Lovera et al., 1991; Harrison et al., 1991) posits that complex diffusion behavior results from argon diffusing from multiple, non-interacting subgrain domains of different sizes that are stable both during the geologic history and laboratory heating of a feldspar. Others have suggested that complex argon diffusion behavior may also arise due to structural modifications, microtextural development, fluid alteration, or some combination therein (e.g., Parsons et al., 1999; Lovera et al., 2002; Villa, 2006; McLaren et al., 2007; Villa and Hanchar, 2013; Cassata and Renne, 2013). In these cases, the timing of various mineralogical changes with respect to the thermal history of a feldspar matter greatly to the interpretation of complex argon diffusion behavior.

For planetary surface paleothermometry using cosmogenic neon, any subgrain alteration during the geologic history of a feldspar will have occurred at higher temperatures than those of interest, but will likely still affect the kinetics of neon diffusion at low temperature. It is thus important to distinguish complex neon behavior due to any existing crystallochemical heterogeneities from that resulting from potential structural changes during laboratory heating. In previous work on noble gas diffusion in quartz (Tremblay et al., 2014b), we made this distinction by examining diffusion of both helium and neon in the same aliquots. If structural alteration during laboratory heating changes diffusion kinetics, we would expect deviations from a linear Arrhenius array to occur at a common temperature for both noble gases. On the other hand, if some stable subgrain property is responsible for complex diffusion behavior, then we anticipate the temperature at which deviation from Arrhenius linearity occurs to differ for different noble gases.

In a similar manner, in this work we present neon stepwise degassing experiments on a subset of the feldspars for which Cassata and Renne (2013) conducted argon stepwise degassing experiments. Cassata and Renne (2013) argued that a combination of temperature-dependent structural transitions and the presence of multiple diffusion domains caused deviations from linear Arrhenius behavior in their experiments. Here, we designed our experiments such that the majority of the neon present was released at temperatures lower than those used by Cassata and Renne (2013) to characterize argon diffusion. As a result, all deviations from linear Arrhenius behavior interpreted by Cassata and Renne (2013) to be a result of structural transitions should be absent from our neon experiments, if their interpretation is correct. We also examined feldspars that exhibit linear Arrhenius behavior for argon diffusion to determine whether simple diffusion behavior is also observed for neon. If simple diffusion behavior is observed for both noble gases in a particular feldspar, it suggests that there is a single diffusion domain with a single diffusion lengthscale, which may equal the physical grain size of the aliquots analyzed. In these cases, our experimental results and those of Cassata and Renne (2013) can be compared with theoretical calculations of argon and neon diffusivities.

In addition to addressing the questions outlined above, we use our experimentally-determined diffusion kinetics to

model the sensitivity of cosmogenic neon diffusion to temperature and exposure duration amongst different feldspars. We use the modeled sensitivities to evaluate the potential for using cosmogenic neon in feldspar to constrain past planetary surface temperatures.

2. METHODS

We conducted neon stepwise degassing experiments on a suite of feldspar samples that span the full range of feldspar compositions from orthoclase to anorthite. Brief sample descriptions including compositions are provided in [Table 1](#); for more detailed information, see [Cassata and Renne \(2013\)](#) and references therein. Samples were irradiated with a 220 MeV proton beam for 5 hours at the Francis H. Burr Proton Therapy Center at the Massachusetts General Hospital. Numerous grains from a given sample were packed together into an Sn foil in order to balance ejection of proton-induced Ne with implantation (e.g., [Shuster et al., 2004](#)). These Sn foils were packaged into HDPE capsules (9.4 mm in diameter, 3.0 in mm height), which were stacked into quartz tubes to form a ~500 mm long cylindrical target; the approximate range of 220 MeV protons in HDPE is 300 mm. A 100 μm thick Pb foil in front of the target stack, in conjunction with the target stack itself, defocuses and scatters the proton beam intensity in attempt to evenly distribute the cross-section flux ([Shuster et al., 2004](#); [Shuster and Farley, 2005a](#)). The target was flipped halfway through the irradiation to ensure Ne production in both ends of the target stack despite proton energy dissipation; the feldspars examined here were located within 150 mm of either end of the target stack. Sample temperatures do not exceed 45 °C during irradiation ([Shuster and Farley, 2005b](#)). Proton irradiation of the feldspars examined here took place in April 2013 with a total proton fluence of $\sim 8.5 \times 10^{15}$ p/cm², which was measured during irradiation by a thin foil transmission ionization chamber in front of the beam aperture.

This irradiation design should lead to spatially uniform Ne production for crystal fragments < 500 μm in radius ([Shuster and Farley, 2005a](#)) if the crystal fragments are compositionally uniform. With the exception of Fish Canyon sanidine and Grass Valley anorthite, the feldspars studied here are compositionally homogeneous with respect to these elements ([Cassata and Renne, 2013](#)) and we therefore expect proton-induced Ne to be spatially uniform. The production of uniform, high concentrations of neon isotopes

from proton irradiation allows us to conduct stepwise degassing experiments on single feldspar crystals ([Shuster et al., 2004](#); [Shuster and Farley, 2005b](#); [Tremblay et al., 2014b](#)). Implications for compositional zonation of Fish Canyon sanidine and Grass Valley anorthite are detailed in the discussion.

The effects of lattice damage from proton irradiation on noble gas diffusion in feldspars has not been explicitly investigated. Previous work empirically demonstrates that lattice damage generated during proton irradiation with the magnitude of fluence and energy used here does not significantly modify noble gas diffusion kinetics in other mineral phases ([Shuster et al., 2004](#); [Shuster and Farley, 2005b](#); [Tremblay et al., 2014a](#)). Although neutron irradiation, which typically has 2–3 orders of magnitude higher fluence than proton irradiation, has been shown to influence noble gas diffusion in apatite ([Shuster and Farley, 2009](#)), several studies have demonstrated that damage generated during neutron irradiation minimally affects argon diffusion kinetics ([Foland and Xu, 1990](#); [Lovera et al., 1993](#); [Cassata and Renne, 2013](#)). Given this set of observations, we therefore assume that damage produced during proton irradiation does not significantly modify neon diffusion kinetics in feldspars, although this assumption should be tested with replicate experiments on aliquots irradiated with different proton fluences and energies.

Proton irradiated feldspars were inspected by binocular microscopy to select individual crystals lacking penetrative fractures and visible inclusions. Selected crystals were photographed to estimate crystal dimensions ([Fig. S1](#)) and then placed under vacuum inside Pt-Ir alloy packets affixed to K-type thermocouples. Packets were heated with either a 30 or 150 W diode laser in a feedback control loop with the thermocouple via a PID temperature controller, enabling us to maintain a setpoint temperature to within 2 °C. Samples were heated in fifty or more consecutive heating steps to temperatures between 100 and 1200 °C. Each heating schedule contained at least two retrograde heating cycles, and individual heating steps lasted between 0.5 and 4 hours. All measurements were made on an MAP 215-50 sector field mass spectrometer in the Noble Gas Thermochronometry Lab of the Berkeley Geochronology Center; gas purification and mass spectrometric measurement techniques are detailed in [Tremblay et al. \(2014b\)](#). For ²¹Ne, we made no isobaric interference corrections; the MAP 215-50 cannot resolve ²⁰Ne¹H from ²¹Ne, and we assume corrections due to this isobaric interference are

Table 1
Description of feldspar samples studied in diffusion experiments.

Sample	Description	Phase	Composition		
			An	Ab	Or
Bmk	Granitic pegmatite, Benson Mines, NY USA	Orthoclase	0.0	3.0	97.0
FCs	Rhyolitic ignimbrite, Fish Canyon Tuff, CO USA	Sanidine	1.0	27.0	72.0
GSS	Rhyolitic ash, Gulf of Salerno, Italy	Sanidine	3.7	30.5	65.8
SURTp	Basaltic lava, Surtsey, Iceland	Labradorite	59.6	39.6	0.8
OREGp	Basaltic lava, Plush, OR USA	Labradorite	63.9	35.4	0.7
GV-09	Anorthosite, Grass Valley, CA USA	Anorthite	94.2	5.2	0.6
76535	Troctolite, Moon	Anorthite	96.2	3.5	0.3

negligible. ^{21}Ne background corrections were made by subtracting the average of six or more room temperature procedural blanks measured over the course of each experiment from measurement time-zero intercepts; the average correction for ^{21}Ne across all experiments was 0.06×10^6 atoms. ^{20}Ne and ^{22}Ne have isobaric interferences from $^{40}\text{Ar}^{++}$ and $^{44}\text{CO}_2^{++}$, respectively, which the MAP 215-50 sector field mass spectrometer used for these experiments also cannot resolve. Although these interferences can be corrected for by introducing an ^{39}Ar spike during neon measurements and observing a linear relationship between the $\text{Ar}^{++}/\text{Ar}^+$ and $\text{CO}_2^{++}/\text{CO}_2^+$ ratios (Balco and Shuster, 2009), we did not use the spike procedure during these experiments. Instead, we assumed that all of the ^{22}Ne signal observed during room-temperature procedural blanks was entirely from $^{44}\text{CO}_2^{++}$ and used the average blank 44/22 ratio and measured $^{44}\text{CO}_2^+$ signals to correct measured ^{22}Ne signals during heating steps. ^{20}Ne was not measured. Experiments were terminated when three or more consecutive heating steps yielded ^{21}Ne and ^{22}Ne time-zero intercepts at or below background level. We determined total neon amounts by comparison with the time-zero intercepts of a manometrically-calibrated air standard. Measurement of different calibrated pipette volumes of the air standard demonstrated that ^{21}Ne sensitivity was constant over the pressure range of the analyses in a given experiment. Blank corrected ^{21}Ne and ^{22}Ne abundances for each heating step are reported in Table S1. The magnitude of the isobaric interference correction on ^{22}Ne signals for individual heating steps varies between 5 and 100%, with an average correction of $\sim 50\%$. These generally large-magnitude corrections propagate into very large ^{22}Ne uncertainties; therefore we do not use the ^{22}Ne data further. The concentrations of ^{21}Ne and ^{22}Ne present in the individual feldspar crystals analyzed ($>10^{12}$ atoms/g) are orders of magnitude greater than any likely combination of atmospheric, cosmogenic, and nucleogenic neon components present prior to proton irradiation, which for terrestrial samples are typically on the order of 10^6 – 10^8 atoms/g (e.g., Kober et al., 2005; Gourbet et al., 2012). We therefore assume that contributions from these components are negligible in comparison to the uniformly distributed, proton-induced neon, and that variations in the $^{21}\text{Ne}/^{22}\text{Ne}$ ratio between different heating steps reflect the very uncertain isobaric interference correction made for ^{22}Ne .

We used the equations of Fechtig and Kalbitzer (1966) to calculate lengthscale-normalized diffusivities (D/a^2) from the fraction of ^{21}Ne measured and duration of each heating step for each stepwise degassing experiment. By using these equations, we make several assumptions. First, we assume that Ne diffusion is both Fickian and isotropic (Crank, 1975). Ar stepwise degassing experiments on cleavage flakes with different lattice orientations indicate isotropic diffusion in feldspars at the temperatures over which we conduct neon step degassing experiments (Cassata and Renne, 2013). Second, we assume that the initial distribution of the diffusant is spatially uniform; proton irradiation should generate Ne uniformly, as discussed above. Third, we assume that each feldspar crystal has a spherical, fixed

geometry. We approximate the spherically equivalent radius of the samples used in our experiments as the radius of a sphere whose surface area to volume ratio equals that of the crystal analyzed. Previous work demonstrates that this assumption is valid for materials with moderate aspect ratios, even for crystals with realistic shapes or irregular geometries (Meesters and Dunai, 2002; Gautheron and Tassan-Got, 2010; Huber et al., 2011).

We first estimated the surface to volume ratio of the crystals from optical microscopy measurements. Since feldspars do not have distinctive crystal habits and frequently bear surface irregularities such as cleavage steps, we had to make simplifying assumptions about the crystal geometries to make these estimates. To overcome this limitation, we obtained accurate surface area to volume ratio and size determinations of the feldspar crystals by X-ray computed tomography. X-ray computed tomography (CT) allows for three-dimensional, nondestructive characterization of geologic samples based on the variable attenuation of X-rays as they travel through different materials (Ketcham and Carlson, 2001). After the stepwise degassing experiments, we extracted each crystal from its packet to look for evidence of fracturing. Intact fragments were mounted on double sided tape and scanned with $3.15 \mu\text{m}$ resolution on the Xradia MicroXCT scanner at the University of Texas at Austin High-Resolution X-ray CT Facility. Using the software Blob3D (Ketcham, 2005), feldspar crystals were segmented from mounting material using a grayscale threshold and separated into individual crystal volumes. We extracted numerous statistics about these volumes, including surface area, volume, aspect ratio, and maximum and minimum axis lengths, and calculated spherically equivalent radii of the crystals for comparison with our first estimates (Table S2).

3. RESULTS

Results of the neon stepwise degassing experiments are reported in Table S1 and plotted in Figs. 1A–6A, where the natural logarithm of calculated diffusivities ($\ln(D/a^2)$, where D is diffusivity and a is the diffusive lengthscale) is shown as a function of inverse temperature. Figs. 1A–6A also show the results from argon stepwise degassing experiments on different grains of the same feldspars reported by Cassata and Renne (2013). Additionally, in Fig. 7 we compare the result of a neon stepwise degassing experiment on a neutron-irradiated crystal of anorthite from lunar troctolite 76535 (Garrick-Bethell et al., 2017) to an ^{37}Ar stepwise degassing experiment on 76535 anorthite reported by Cassata and Renne (2013). For both neon and argon datasets, we use the Monte Carlo approach described by Tremblay et al. (2014b) to propagate uncertainties in gas release fraction into calculated diffusivities. If the temperature dependence of noble gas diffusion is Arrhenian and the feldspar analyzed is characterized by a single diffusion domain, then we expect to observe a linear correlation in this plotting space. In many cases we observe significant deviations from linearity; however, for all stepwise degassing experiments at least a subset of the data collected comprises a linear array. We fit least squares regressions to

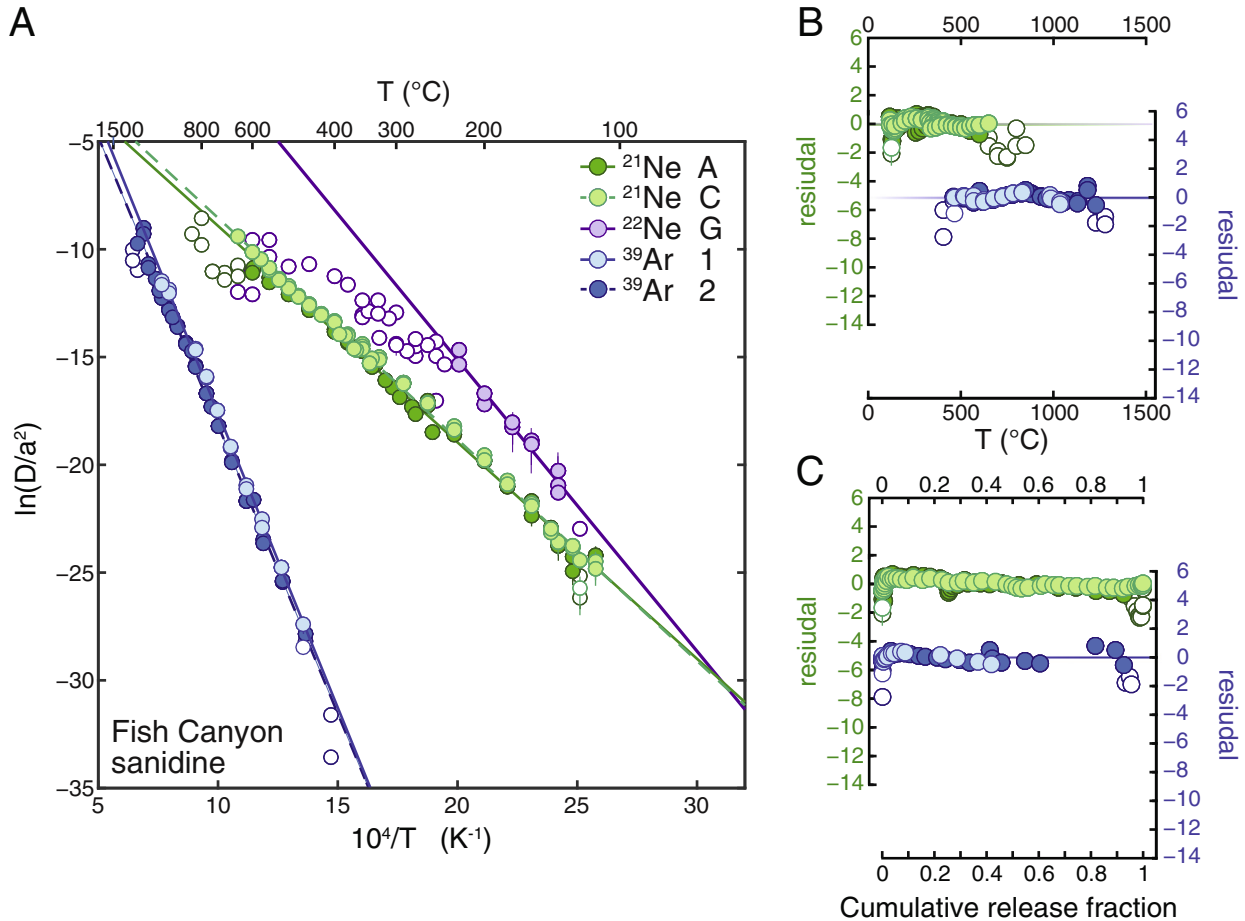


Fig. 1. Arrhenius plot (A) and residual plots (B and C) for diffusion of proton-induced ²¹Ne (green), neutron-induced ³⁹Ar (blue; data from Cassata and Renne, 2013), and neutron-induced ²²Ne (purple; data from Gourbet et al., 2012) in different crystals of Fish Canyon sanidine. For visual clarity, residuals are not shown for neutron-induced ²²Ne. D/a^2 values are normalized to s⁻¹. Uncertainties in $\ln(D/a^2)$ estimated using a Monte Carlo approach (Tremblay et al., 2014b) are shown, although in most cases the uncertainty is smaller than the symbol plotted. Linear regressions in (A) are fit through the filled symbols and used to determine E_a and $\ln(D_0/a^2)$, assuming an Arrhenian dependence of diffusivity on temperature (Eq. (1)). Residuals, defined as the difference between the calculated $\ln(D/a^2)$ from a given heating step and the expected $\ln(D/a^2)$ from the linear regression at the same temperature, are plotted against temperature (B) and cumulative gas release fraction (C). Filled symbols are the same as in (A). (For interpretation of the references to colour in this figure legend, the reader is referred to the web version of this article.)

these subsets in Figs. 1A–7A, with the goal of including as many temperature steps as possible in the regression while minimizing the residuals between the regression and the data. We used these regressions and the Monte-Carlo derived uncertainties in D/a^2 to estimate the activation energy (E_a) and diffusion coefficient (D_0/a^2) from the slope and intercept of the linear regression, respectively, assuming an Arrhenius dependence of diffusivity on temperature:

$$\frac{D}{a^2} = \frac{D_0}{a^2} \exp\left(\frac{-E_a}{RT}\right)$$

where R is the gas constant and T is absolute temperature. These calculated diffusion parameters are reported in Table 2. While the significance of these calculated diffusion parameters is in some cases uncertain, as will be discussed below, fitting these regressions allows us to compare the temperatures and gas fractions over which linear Arrhenius behavior is observed. These comparisons are shown in

Figs. 1B–7B and 1C–7C as residuals, which we define as the difference between the calculated diffusivity from a given heating step and the expected diffusivity from the linear regression at the same temperature.

The two neon stepwise degassing experiments we conducted on Fish Canyon sanidine exhibited single linear Arrhenius arrays over the duration of the experiment, which was also observed in replicate argon stepwise degassing experiments (Fig. 1). Deviation from linearity occurs at the end of neon experiment A; however, this deviation comprises less than 7% of the cumulative ²¹Ne released (Fig. 1C), and the remaining steps do not form any clear additional linear arrays (Fig. 1A). Interestingly, our stepwise degassing experiments using proton-induced ²¹Ne disagree significantly with the experiment using neutron-induced ²²Ne reported by Gourbet et al. (2012), which showed complex neon diffusion behavior (Fig. 1A). Neon and argon stepwise degassing experiments on Gulf of Sale-

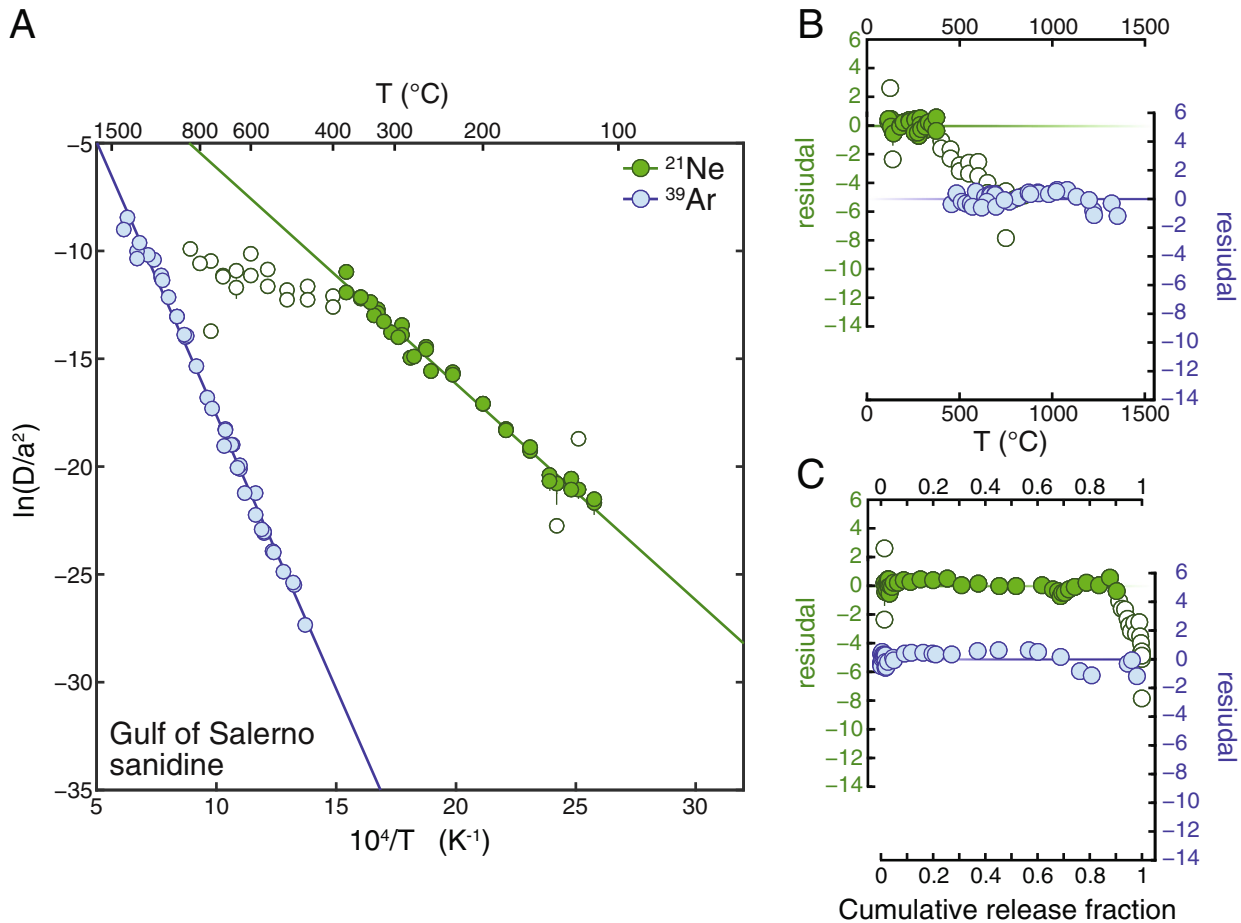


Fig. 2. Arrhenius plot (A) and residual plots (B and C) for diffusion of proton-induced ^{21}Ne (green) and neutron-induced ^{39}Ar (blue; data from Cassata and Renne, 2013) in different crystals of Gulf of Salerno sanidine. Units, uncertainties, linear regressions, and residuals are as described for Fig. 1. (For interpretation of the references to colour in this figure legend, the reader is referred to the web version of this article.)

rno sanidine likewise exhibit simple, linear Arrhenius behavior (Fig. 2). Although several of the high-temperature steps in the neon stepwise degassing experiment deviate from a linear Arrhenius array (Fig. 2B), these steps constitute less than 10% of the cumulative ^{21}Ne released (Fig. 2C) and do not form any clear additional linear arrays (Fig. 2A).

Feldspars other than sanidine exhibit disparate neon and argon Arrhenius behavior. The neon experiment on Benson Mines orthoclase shows a clear downward deviation from linear Arrhenius behavior at $\sim 70\%$ of the cumulative ^{21}Ne release fraction (Fig. 3A and C). A second linear Arrhenius array, which includes a retrograde heating cycle, is observed at higher ^{21}Ne release fractions (Fig. 3A). For comparison, we show the results of an ^{39}Ar stepwise degassing experiment reported by Cassata and Renne (2013) on an equant crystal of Benson Mines orthoclase with an estimated spherical radius equal to that in the neon experiment. The ^{39}Ar experiment appears to comprise a single linear Arrhenius array (Fig. 3A). There is a slight downward deviation in diffusivity between 50 and 70% of the cumulative ^{39}Ar released as well (Fig. 3C). However, the

steps following this downward deviation occur at temperatures exceeding 1100°C (Fig. 3B), at which point the crystal used in the ^{39}Ar experiment is melting (Schaerer, 1950; Parsons, 2010). The two labradorite samples studied from Surtsey, Iceland and Plush, Oregon, both exhibit upward deviations from linear Arrhenius behavior in ^{37}Ar stepwise degassing experiments at temperatures between 600 and 800°C and at gas release fractions $< 10\%$ (Figs. 4 and 5; Cassata and Renne, 2013). Essentially all of the ^{21}Ne in our stepwise degassing experiment on Surtsey labradorite was released during steps below 600°C (Fig. 4C) and comprises a single linear Arrhenius array (Fig. 4A). The ^{21}Ne step degassing experiment on Plush labradorite, on the other hand, shows a significant downward deviation from an initial linear Arrhenius array at 350°C and 25% of the cumulative ^{21}Ne released (Fig. 5). Lastly, we compare neon and argon degassing experiments on two samples of anorthite, the calcium endmember of plagioclase feldspar. In Grass Valley anorthite, neon and argon both show downward deviations from linear Arrhenius behavior, but at different temperatures and gas release fractions (Fig. 6). Anorthite from lunar sample 76535 shows linear Arrhenius

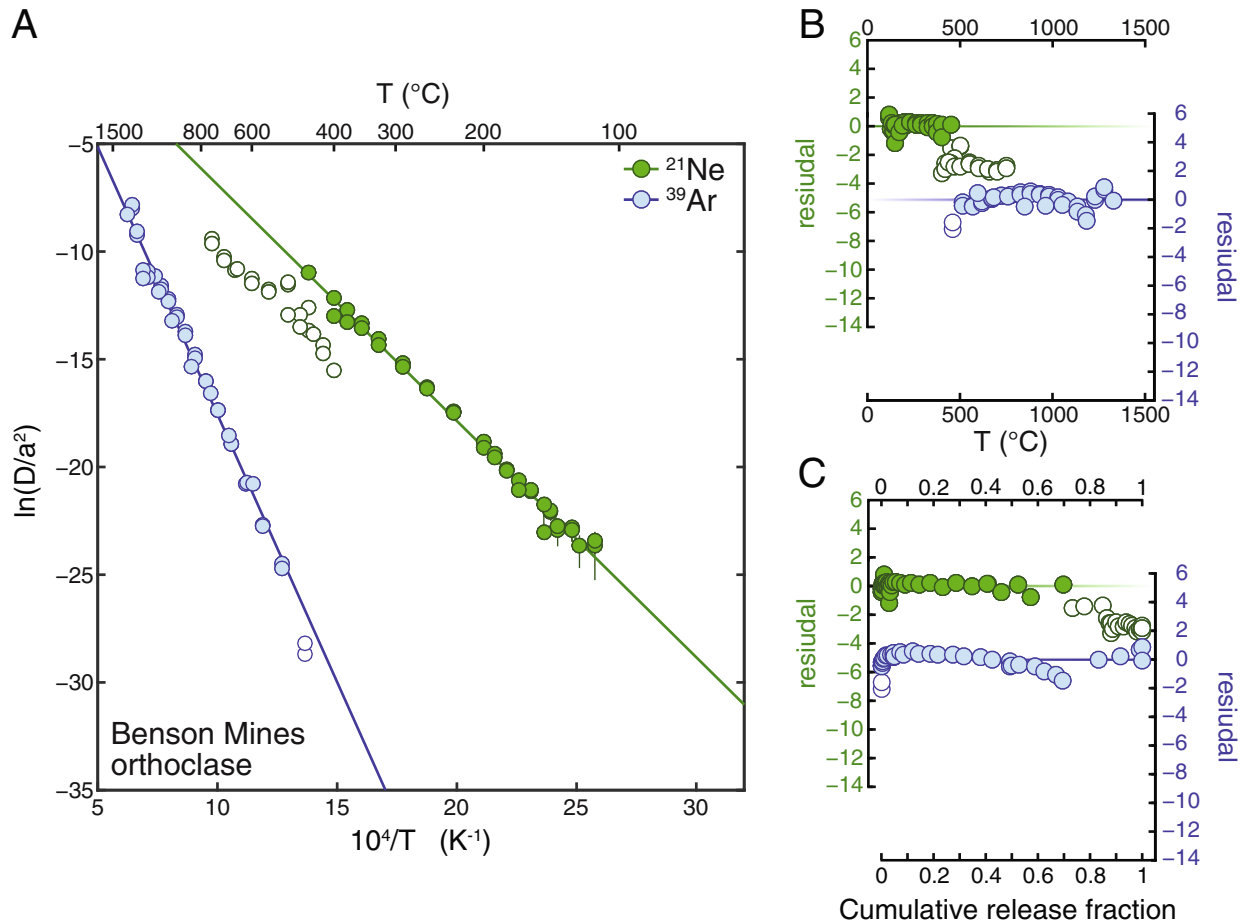


Fig. 3. Arrhenius plot (A) and residual plots (B–C) for diffusion of proton-induced ²¹Ne (green) and neutron-induced ³⁹Ar (blue; data from Cassata and Renne, 2013) in different crystals of Benson Mines orthoclase. Units, uncertainties, linear regressions, and residuals are as described for Fig. 1. (For interpretation of the references to colour in this figure legend, the reader is referred to the web version of this article.)

behavior for 97% of the ²¹Ne measured but downward deviation from linear behavior at 30% of the cumulative ³⁷Ar and 1000 °C.

For the subset of each dataset comprising a linear Arrhenius array, we find that ²¹Ne activation energies range from 83.3 to 110.7 kJ/mol and apparent pre-exponential factors (D_0) range from 2.4×10^{-3} to 1.99×10^2 cm² s⁻¹. These diffusion parameters are within the range of those calculated by Gourbet et al. (2012) for three alkali feldspars. Activation energies and apparent pre-exponential factors for ²¹Ne diffusion in plagioclase feldspars are generally greater than those in alkali feldspars, although a larger number of neon stepwise degassing experiments are necessary to determine if this trend is systematic. Roughly the opposite trend was observed for the activation energy of argon diffusion as a function of composition (Cassata and Renne, 2013).

4. DISCUSSION

While argon diffusion in feldspars has been studied at length over several decades, this is only the second work to examine neon diffusion in feldspars and the first work

to study neon diffusion in plagioclase feldspars. As such, these neon stepwise degassing experiments provide insight into the potential noble gas diffusion mechanisms in feldspars. Below we discuss evidence for both structural modifications and multiple diffusive lengthscales affecting noble gas diffusion in feldspars. For feldspars that exhibit complex neon diffusion behavior, we construct multiple diffusion domain (MDD) models. We use the diffusion parameters from these MDD models as well as the diffusion parameters determined for feldspars exhibiting simple Arrhenius behavior to explore the temperatures and exposure durations over which cosmogenic neon-in-feldspar paleothermometry can be applied to study past surface temperatures.

4.1. Comparison of neon and argon diffusion

4.1.1. Neon and argon diffusion in alkali feldspars

Of the samples we examined, Fish Canyon and Gulf of Salerno sanidine exhibited the simplest Arrhenius behavior for argon diffusion (Figs. 1 and 2; Cassata and Renne, 2013). A single linear Arrhenius array characterizing all of the ³⁹Ar released during these experiments is consistent

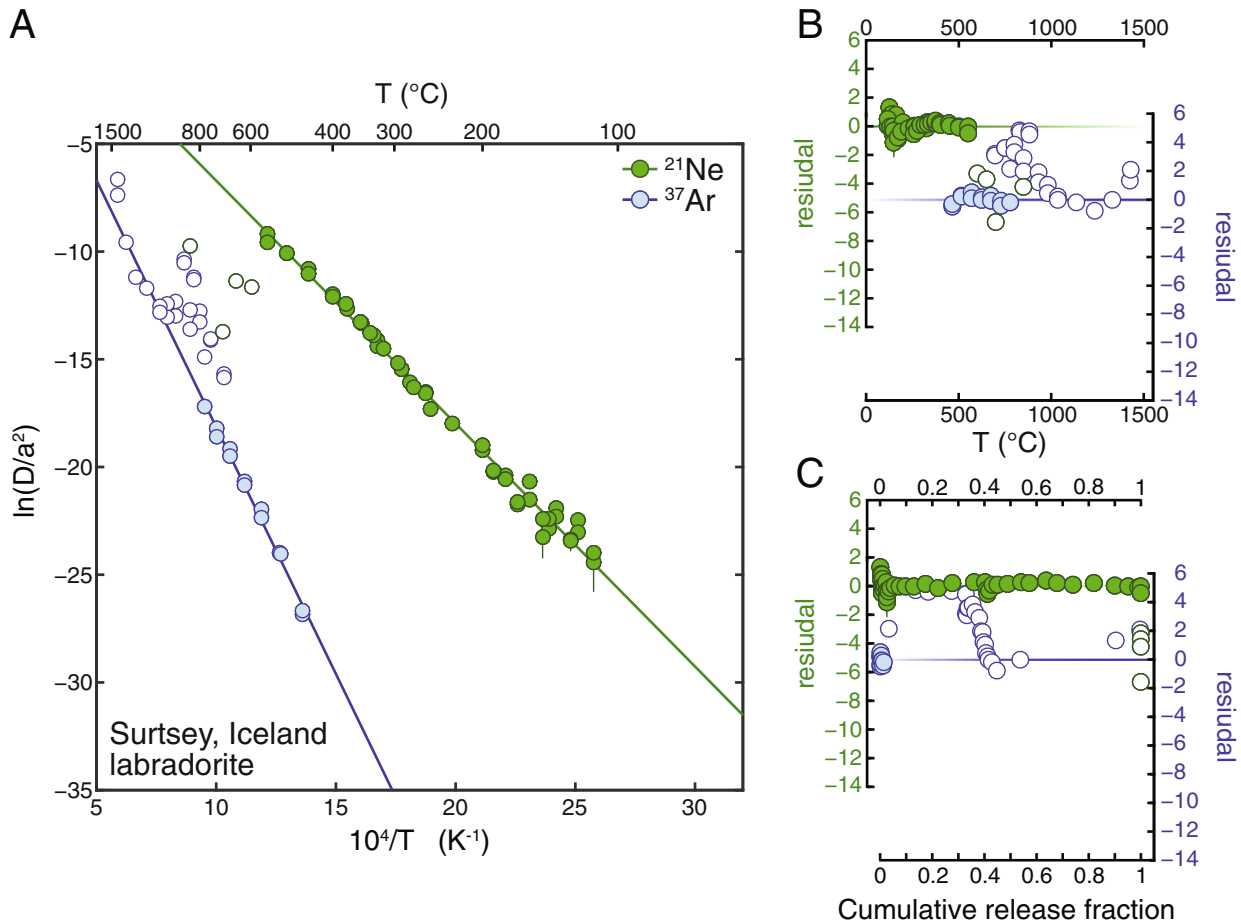


Fig. 4. Arrhenius plot (A) and residual plots (B and C) for diffusion of proton-induced ^{21}Ne (green) and neutron-induced ^{37}Ar (blue; data from Cassata and Renne, 2013) in different crystals of Surtsey, Iceland labradorite. Units, uncertainties, linear regressions, and residuals are as described for Fig. 1. (For interpretation of the references to colour in this figure legend, the reader is referred to the web version of this article.)

with a single diffusion lengthscale, which we assume is equal the grain size analyzed (in which case $a \approx 213$, 332, and 407 μm for Fish Canyon sanidine 1, Fish Canyon sanidine 2, and Gulf of Salerno sanidine respectively, which we estimated from the total amount of ^{39}Ar , the duration of the neutron irradiation, and the stoichiometry of each feldspar). Cassata and Renne (2013) also attribute simple behavior to the fact that sanidine has monoclinic crystal symmetry at room temperature and does not undergo a displacive transition during heating. Consequently, thermal expansion proceeds linearly in all three unit cell directions (Brown et al., 1984; Hovis et al., 1999). Our proton-induced ^{21}Ne stepwise degassing experiments on Fish Canyon and Gulf of Salerno sanidine also exhibit simple diffusion behavior, with $\geq 90\%$ of the ^{21}Ne degassed plotting on a single linear Arrhenius array and no additional arrays formed from the few high temperatures steps that deviate. The neutron-induced ^{22}Ne stepwise degassing experiment on Fish Canyon sanidine reported by Gourbet et al. (2012) seemingly conflicts with our observation of simple neon diffusion behavior (Fig. 1A). One possibility is that the crystal fragment used in the neutron-irradiated experiment was fractured before or during the stepwise degassing

experiment. Another possibility is that heating to >250 $^\circ\text{C}$ during neutron irradiation caused some diffusive loss of neon. This latter possibility seems likely given the diffusion kinetics we determined for Fish Canyon sanidine; however, we would expect the initial neon data from the neutron-irradiated experiment to plot below the linear Arrhenius array in the proton-irradiated experiment if this were the case. Gourbet et al. (2012) suggest that production of ^{22}Ne from the spallation reaction $^{23}\text{Na}(n,np)^{22}\text{Ne}$ during neutron irradiation may have been spatially variable due to core-to-rim zonation of Na in Fish Canyon sanidine (Bachmann et al., 2002). Spatially variable ^{22}Ne production violates the assumption of a uniform initial ^{22}Ne distribution and could lead to curved Arrhenius arrays. However, if spatially variable production of ^{22}Ne from ^{23}Na was the cause of nonlinear behavior, we would expect to observe nonlinear behavior in the argon experiments as well, given that ^{39}Ar is produced from ^{39}K and K is also zoned in Fish Canyon sanidine (Bachmann et al., 2002). Curvature in the proton-irradiated neon experiments might also be expected if this were the case, although spatially variable production from ^{23}Na would be buffered by reactions on Al and Si with similar cross sections (Koning et al., 2015). Given these

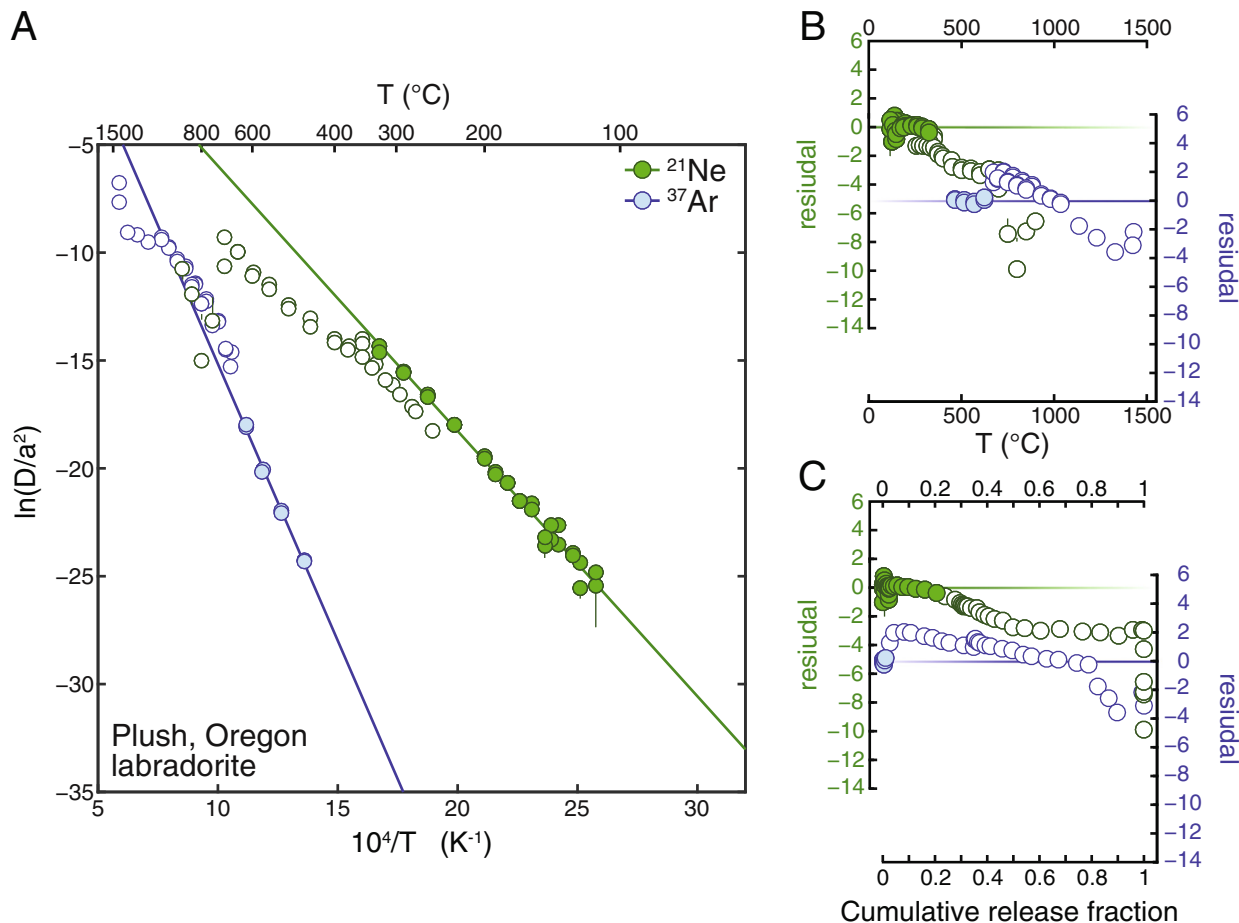


Fig. 5. Arrhenius plot (A) and residual plots (B and C) for diffusion of proton-induced ^{21}Ne (green) and neutron-induced ^{37}Ar (blue; data from Cassata and Renne, 2013) in different crystals of Plush, Oregon labradorite. Units, uncertainties, linear regressions, and residuals are as described for Fig. 1. (For interpretation of the references to colour in this figure legend, the reader is referred to the web version of this article.)

numerous potential complications with the Fish Canyon sanidine experiment reported by Gourbet et al. (2012), we suggest that our stepwise degassing experiments using proton-irradiated Fish Canyon sanidine more accurately characterize neon diffusion in that sample. Our ^{21}Ne results, when paired with the ^{39}Ar stepwise degassing experiments, strongly support the case for these sanidine samples having a single diffusion domain with a single diffusion lengthscale, which we assume is defined by the physical grain size. Additionally, the diffusion parameters (E_a and D_0) for Fish Canyon and Gulf of Salerno sanidine are in good agreement with one another for the respective noble gases examined. The diffusion parameters reported in Table 2 for Fish Canyon and Gulf of Salerno sanidine can therefore be straightforwardly compared to theoretical calculations (e.g., density functional theory or molecular dynamics simulations) of interstitial neon and argon diffusion through the monoclinic sanidine crystal structure.

The Arrhenius behavior of ^{21}Ne diffusion in Benson Mines orthoclase is somewhat surprising, as monoclinic orthoclase is also expected to undergo linear thermal expansion. Cassata and Renne conducted five argon stepwise degassing experiments on Benson Mines orthoclase, one

on an equant fragment (Fig. 3) and four on sheet-like cleavage fragments (Fig. S2). All five experiments exhibit deviations from a linear Arrhenius array at high temperatures and ^{39}Ar release fractions; however, in all experiments these deviations occur near the melting point of orthoclase (Schairer, 1950; Parsons, 2010), making it difficult to assess its origin. The ^{21}Ne stepwise degassing experiment on Benson Mines orthoclase, on the other hand, shows a clear downward deviation from linear Arrhenius behavior beginning at 70% of the cumulative ^{21}Ne released and at 500 $^\circ\text{C}$, hundreds of degrees below the melting temperature of orthoclase (Fig. 3). There was no visible evidence for fracturing or other alteration when we unpacked the crystal for X-ray CT analysis, indicating that no change in the physical grain size occurred before or during the experiment. Additionally, a second linear Arrhenius array observed at higher temperatures and gas release fractions in the ^{21}Ne experiment includes a retrograde heating cycle (Fig. 3A). If nonlinear Arrhenius behavior resulted from a reversible, temperature-dependent structural transformation, we would expect diffusivities in the retrograde heating to approach diffusivities observed at the same temperatures in the preceding prograde heating, which was not observed.

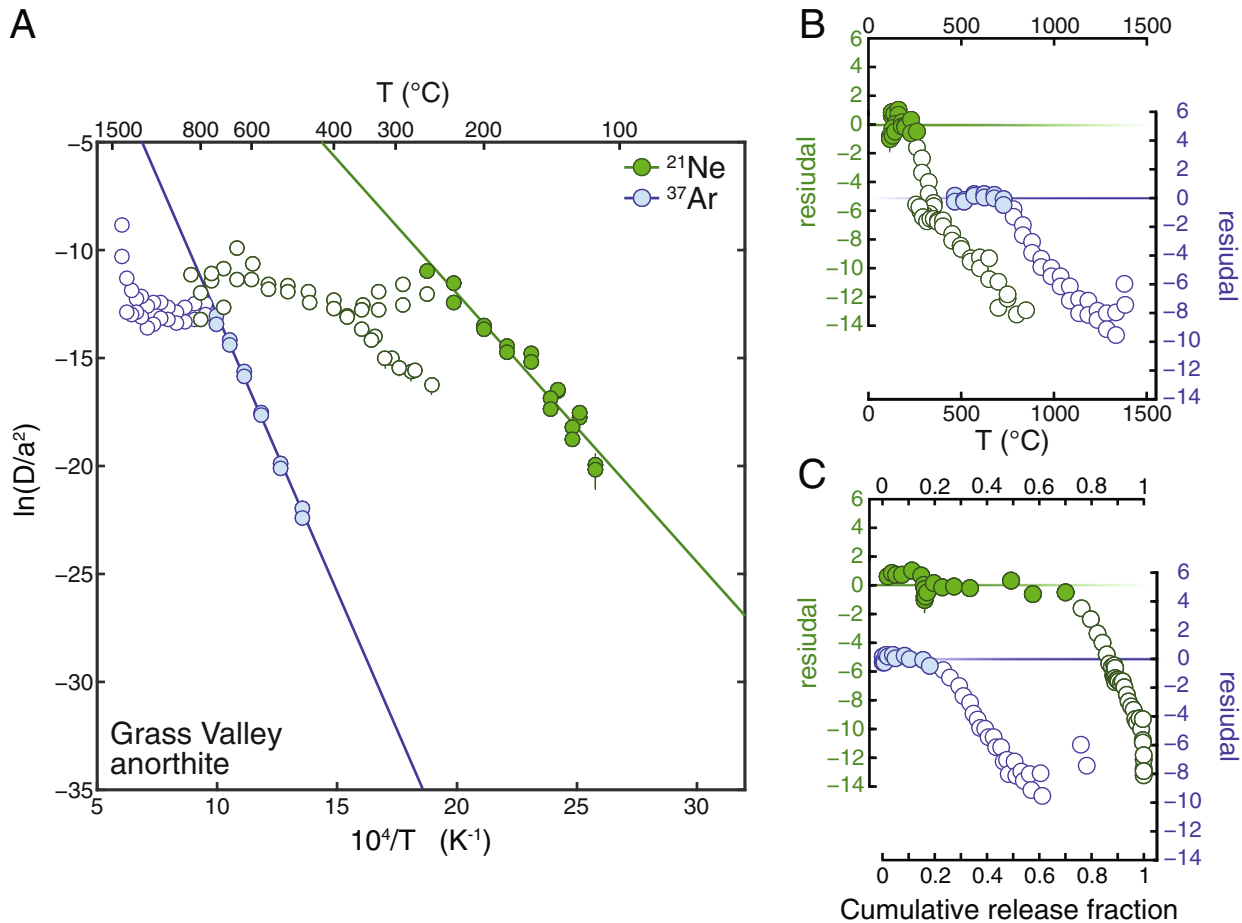


Fig. 6. Arrhenius plot (A) and residual plots (B and C) for diffusion of proton-induced ^{21}Ne (green) and neutron-induced ^{37}Ar (blue; data from Cassata and Renne, 2013) in different crystals of Grass Valley anorthite. Units, uncertainties, linear regressions, and residuals are as described for Fig. 1. (For interpretation of the references to colour in this figure legend, the reader is referred to the web version of this article.)

These observations leave two potential explanations for the nonlinear Arrhenius behavior. It is possible that the crystal of Benson Mines orthoclase we analyzed was fractured in a way that was not detected by either optical microscopy or X-ray CT, in which case replicating the neon step degassing experiment on a different crystal of Benson Mines orthoclase would result in different Arrhenius behavior. Alternatively, these results could indicate that nonlinear Arrhenius behavior of ^{21}Ne reflects a preexisting material property (sub-grain domain distribution) of Benson Mines orthoclase. This latter possibility suggests that the same intrinsic property of Benson Mines orthoclase ought to cause nonlinear Arrhenius behavior for argon. Deviations from linearity observed in argon experiments reported by Cassata and Renne (2013) occur between 15 and 80% of the Ar released, which at first appears to suggest that sub-grain features defining the diffusion lengthscale vary from grain to grain. However, these deviations all occur near the melting temperature of orthoclase, making the origin of these deviations ambiguous. A straightforward test of this hypothesis would be to conduct another ^{39}Ar stepwise degassing experiment on Benson Mines orthoclase with a revised heating schedule, such that all of the ^{39}Ar is released

at temperatures significantly below the orthoclase melting temperature.

4.1.2. Neon and argon diffusion in plagioclase feldspars

Our neon stepwise degassing experiments on plagioclase feldspars highlight how the effects of both structural modification during laboratory heating and preexisting material properties can be convoluted to result in nonlinear Arrhenius behavior. Cassata and Renne (2013) conducted a number of experiments on labradorite samples, all of which exhibit upward deviations from initial linear Arrhenius arrays at temperatures between 600 and 800 $^\circ\text{C}$. They argue that in labradorite and other Ca-rich feldspars, upward deviations are the result of an increase in the rate of thermal expansion above 600 $^\circ\text{C}$, which has been observed experimentally (Tribaudino et al., 2010; Hovis et al., 2010). This interpretation is consistent with our neon stepwise degassing experiments on Surtsey and Plush labradorite, as we observed no upward deviations from an initial Arrhenius array and degas >99% of the ^{21}Ne below 600 $^\circ\text{C}$ in both experiments (Figs. 4 and 5). However, in the case of Plush labradorite, we observe a downward deviation from an initial linear Arrhenius array when $\sim 25\%$ of the ^{21}Ne had

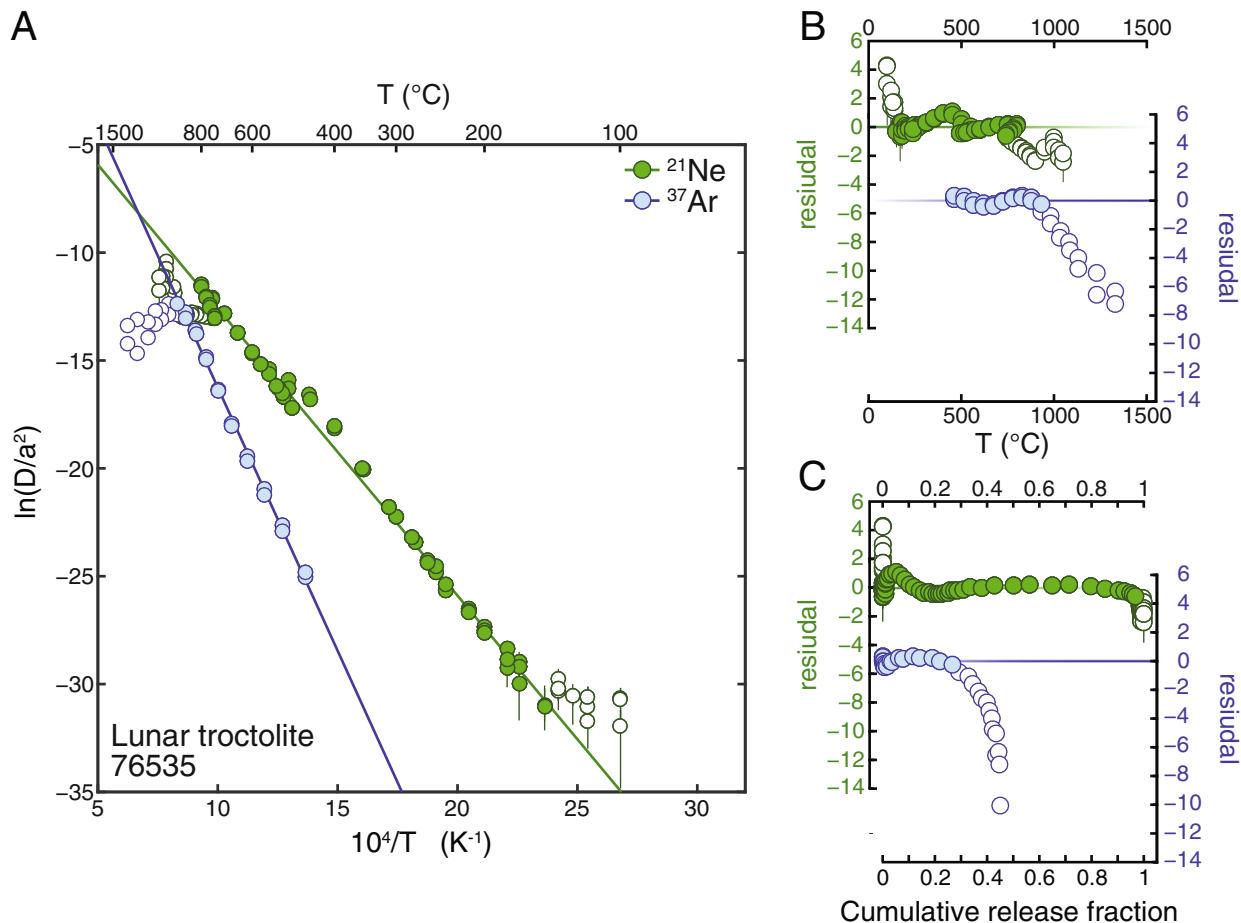


Fig. 7. Arrhenius plot (A) and residual plots (B and C) for diffusion of neutron-induced ²¹Ne (green; data from Garrick-Bethell et al., 2017) and ³⁹Ar (blue; data from Cassata and Renne, 2013) in different crystals of lunar 76535 anorthite. Units, uncertainties, linear regressions, and residuals are as described for Fig. 1. (For interpretation of the references to colour in this figure legend, the reader is referred to the web version of this article.)

Table 2
Summary of neon diffusion parameters. 1 σ uncertainties are reported.

Sample	Spherical equiv. radius (μm) ^a	E_a (kJ/mol)	\pm	$\ln(D_0/a^2)$	\pm	Apparent D_0 (cm ² /s) ^b
BMk-D	283, 271	91.7	2.1	4.32	0.44	5.52×10^{-2}
FCs-A	308, 276	83.6	1.8	1.14	0.34	2.38×10^{-3}
FCs-C	327, 328	86.3	1.4	1.90	0.24	7.19×10^{-3}
GSs-A	178, 205	83.3	1.5	3.88	0.32	2.04×10^{-2}
SURTp-B	307	94.3	1.2	4.72	0.24	1.06×10^{-1}
OREGp-A	320, 336	102.1	1.9	6.28	0.46	6.03×10^{-1}
GV-09-A	230	103.3	3.5	12.84	0.89	1.99×10^2
76535-B ^c	296, 244	110.7	1.6	0.73	0.32	8.86×10^{-1}

^a Spherically equivalent radii were calculated in several different ways. In the first instance, the radius was calculated from the surface area to volume ratio (SA/V) of the crystal analyzed using optical microscope measurements. For some of the ²¹Ne stepwise degassing experiments, a second radius is listed that was calculated from the SA/V determined from X-ray computed tomography measurements (Table S2).

^b Calculated assuming the spherically equivalent radius of the crystals analyzed defines a , the diffusive lengthscale.

^c Stepwise degassing experiment data presented in Garrick-Bethell et al. (2017).

been released and at 350 °C (Fig. 5), a temperature for which no changes in the rate of thermal expansion are expected. Like our neon degassing experiment on Benson Mines orthoclase, retrograde heating steps in the Plush lab-

radorite experiment do not overlap with the initial linear Arrhenius array, confirming that this behavior is not a result of a reversible structural change. If we assume that the crystal of Plush labradorite was not fractured, these

results instead suggest that complex neon diffusion behavior reflects a preexisting material property of Plush labradorite. A very small fraction (<10%) of the total gas is released below 600 °C in argon stepwise degassing experiments; therefore the effects of this preexisting material property are likely obscured by the coincident changes in rate of thermal expansion. Without the observation of temperature-independent complex Arrhenius behavior from the neon stepwise degassing experiment on Plush labradorite, simple down-temperature extrapolation of the initial linear Arrhenius array in the argon stepwise degassing experiment to geologically relevant temperatures may have seem justified. However, doing so would likely result in inaccurate thermal history reconstruction. In contrast to Plush labradorite, with Surtsey labradorite we observe a single linear Arrhenius array for ^{21}Ne (Fig. 4), suggesting this labradorite is characterized by a single diffusion domain with a single diffusion lengthscale, which may be defined by the physical grain size ($a \approx 307 \mu\text{m}$). Furthermore, this implies that nonlinear behavior for Ar diffusion, manifest as upward curvature on Arrhenius plots at ~ 600 °C, followed by downward curvature at higher temperatures, is likely related to structural modifications of the feldspar in response to heating (Cassata and Renne, 2013). Accurate geologic thermal history information could therefore be inferred for Surtsey labradorite by downward extrapolation of initial linear Arrhenius arrays.

Unlike the other feldspars we studied, anorthite undergoes a structural transition during neon stepwise degassing experiments. Between 225 and 300 °C, anorthite transitions from a *PI* to *T* triclinic crystal symmetry (Smith and Ribbe, 1969; Van Tendeloo et al., 1989). The *PI*–*T* transition is accompanied by an increase in unit cell volume and in the rate of thermal expansion (Tribaudino et al., 2010), both of which ought to decrease the energy barrier to interstitial diffusion and increase noble gas diffusivities. Therefore we expect to observe upward deviations from initial linear Arrhenius arrays associated with this transition in neon stepwise degassing experiments but not in argon stepwise degassing experiments, as the latter take place at temperatures above the *PI*–*T* transition. In the ^{21}Ne stepwise degassing experiment on Grass Valley anorthite, we observed the opposite: downward deviation from an initial linear Arrhenius array occurred at 300 °C (Fig. 6). However, we do not find this surprising given the crystallochemical complexity of Grass Valley anorthite, which is characterized by two phases of anorthite separated by antiphase boundaries, as well large muscovite inclusions, plagioclase subgrains, and Na-rich feldspar alteration patches (McLaren and Marshall, 1974; Rainey and Wenk, 1978). Thus we anticipate both the diffusion kinetics and initial distribution of neon to be spatially variable in this sample. Given this heterogeneity, it is also expected that the argon and neon diffusion experiments on different aliquots of Grass Valley anorthite are not reconcilable with one another. A neon stepwise degassing experiment on neutron-irradiated anorthite from lunar sample 76535 (Garrick-Bethell et al., 2017) exhibits linear Arrhenius behavior between 170 and 800 °C for essentially all of the gas released (Fig. 7). There appears to be a slight upward deviation in the diffusivities at

~ 300 °C, which may be associated with the *PI*–*T* transition. However, fitting a linear regression to only the data collected below 300 °C yields indistinguishable diffusion parameters from those calculated using all the data. Linear Arrhenius behavior at temperatures below 800 °C in the neon experiment is also consistent with the downward deviation from an initial linear Arrhenius array above 800 °C in the argon experiment being caused by the transition to an *II* symmetry (Megaw et al., 1962; Foit and Peacor, 1973).

To summarize our comparison of neon and argon stepwise degassing experiments, we often see different Arrhenius behavior for neon diffusion than was observed for argon diffusion in the same feldspars. The origin of these differences depends on the feldspar in question. In several cases, the effects of a preexisting material property of a particular feldspar and the effects of a structural transformation during laboratory heating are conflated in argon stepwise degassing experiments; neon stepwise degassing experiments conducted at lower temperatures make such confluences apparent. It would be valuable to measure neon and argon isotopes simultaneously in future stepwise degassing experiments on neutron-irradiated feldspars in order to discern between such effects.

4.2. Multiple diffusion domain (MDD) model for neon diffusion in feldspars

At present, we cannot ascribe a specific intrinsic property or mechanism to nonlinear Arrhenius behavior that is not associated with a temperature-dependent structural transformation. Identifying the origin of this complex Arrhenius behavior in argon stepwise degassing experiments is critically important, because crystallochemical changes that could potentially be responsible for this behavior (e.g., strain-induced microtextural development, fluid alteration) may have occurred during the portion of a sample's geologic thermal history that is relevant to $^{40}\text{Ar}/^{39}\text{Ar}$ thermochronometry. For cosmogenic noble gas thermochronometry using neon in feldspars, wherein production and diffusion are only happening at planetary surfaces where feldspars are exposed to cosmic ray particles, we expect any major crystallochemical changes to have occurred at much higher temperatures than are relevant to the system of interest. In other words, all crystallochemical heterogeneities are present throughout the thermal history recorded by cosmogenic neon in feldspars, with the possible exception of those generated by shock during impact events. Thus although we do not have a mechanistic explanation for the nonlinear, temperature-independent Arrhenius behavior observed in some neon experiments, we think this complex behavior characterizes cosmogenic neon diffusivity and therefore must be accounted for to accurately reconstruct temperatures using cosmogenic neon in feldspars.

In order to account for complex neon diffusion in feldspars, we modeled the results of stepwise degassing experiments exhibiting complex Arrhenius behavior using multiple diffusion domain (MDD) theory (Lovera and Richter, 1989; Lovera et al., 1991; Harrison et al., 1991). MDD theory explains nonlinear Arrhenius behavior as

the result of diffusion from multiple, non-interacting sub-grain domains of varying sizes. Our modeling approach is similar to that described in Tremblay et al. (2014b), wherein diffusivities are calculated for the experiment heating sched-

ule using the equations outlined by Fechtig and Kalbitzer (1966) for a spherical geometry and for a given diffusion domain distribution. The number of subgrain domains was allowed to vary, and the models were designed to search over a large number of combinations of activation energy (E_a), pre-exponential factor (D_0/a^2), and gas fraction (f) attributed to each domain; activation energy was held in common for all domains. For a particular number of diffusion domains, we determined the combination of diffusion parameters and gas fractions that best agreed with the stepwise degassing experiments by calculating a misfit statistic M :

$$M = \sum_{j=1}^n |f_{p,j} - f_{m,j}|$$

where $f_{p,j}$ is the modeled cumulative ^{21}Ne released at heating step j , $f_{m,j}$ is the observed cumulative ^{21}Ne released at heating step j , and n is the total number of heating steps. This misfit statistic is analogous to the reduced chi-squared misfit statistic used in Tremblay et al. (2014b) in that the same set of diffusion parameters minimizes both quantities. However, the cumulative difference in predicted and observed gas fractions used here has more physical meaning. For example, a misfit statistic of 0.15 can be thought of as not predicting 15% of the observed ^{21}Ne released with our MDD model. We continued to add diffusion domains until the minimized misfit statistic with $x + 1$ domains was within 0.03 of the minimized misfit statistic with x domains. In Fig. 8, we show the best fit MDD models for the neon stepwise degassing experiments on Benson Mines orthoclase, Plush labradorite, and Grass Valley anorthite; best fit diffusion parameters, gas fractions, and misfit statistics are reported in Table 3. By assuming that this model framework can be extrapolated over time and to lower temperatures, we use the MDD model fits for these feldspars in the remaining discussion to assess the sensitivity of cosmogenic neon-in-feldspar paleothermometry to exposure temperature and duration.

4.3. Implications for neon retentivity in feldspars

The seven neon stepwise degassing experiments reported here, combined with the experiments reported by Gourbet et al. (2012) and Garrick-Bethell et al. (2017), demonstrate that neon diffusion kinetics and behavior vary widely amongst feldspars of different compositions and geologic origins. This is perhaps not surprising, given the vast range of diffusion kinetics and behavior observed in argon

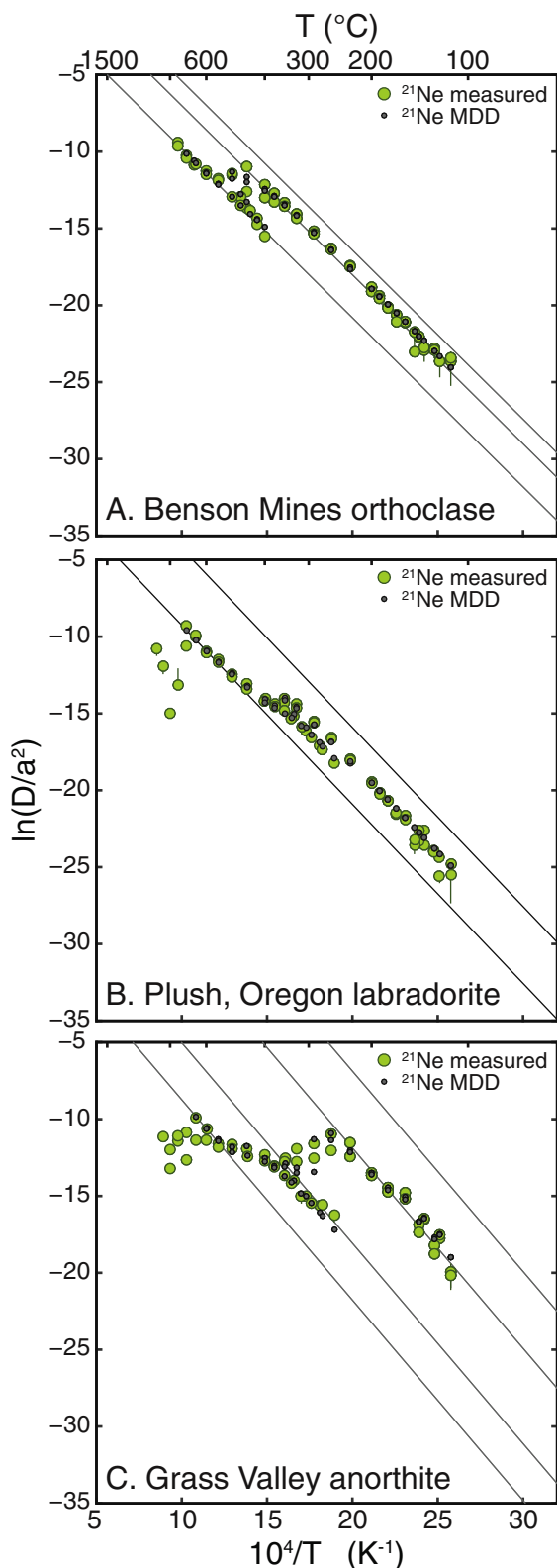


Fig. 8. Arrhenius plots comparing calculated diffusivities from multiple diffusion domain (MDD) models (black) to calculated diffusivities from neon stepwise degassing experiments (green) for Benson Mines orthoclase (A), Plush labradorite (B), and Grass Valley anorthite (C). Lines correspond to diffusion parameters characterizing each diffusion domain, which are listed in Table 3 along with the fraction of gas comprising each domain and the misfit statistic of the models shown. (For interpretation of the references to colour in this figure legend, the reader is referred to the web version of this article.)

Table 3
Best fit multiple diffusion domain model parameters.

Sample	Domain	E_a (kJ/mol)	$\ln(D_0/a^2)$	f	Misfit
BMk-D	1	91.5	4.0	0.45	0.17
	2		5.6	0.30	
	3		1.2	0.25	
OREGp-A	1	96.9	2.4	0.74	0.16
	2		7.4	0.26	
GV-09-A	1	108.4	14.9	0.76	0.33
	2		19.2	0.08	
	3		8.0	0.08	
	4		4.3	0.08	

stepwise degassing experiments (e.g., [Lovera et al., 1997, 2002](#); [Cassata and Renne, 2013](#)). Nonetheless, the variability of neon diffusion kinetics and behavior has important implications for the applicability of laboratory-determined diffusion kinetics to applications of cosmogenic neon paleothermometry ([Tremblay et al., 2014a](#)). Specifically, these results indicate that sample-specific diffusion kinetics will be necessary to quantitatively reconstruct temperatures using cosmogenic neon in feldspars.

To illustrate this point, in [Fig. 9](#) we show how cosmogenic neon retentivity will evolve as a function of exposure duration for a constant exposure temperature of 20 °C using the different diffusion parameters obtained in neon stepwise degassing experiments. Retentivity refers to the amount of cosmogenic neon produced during exposure to cosmic ray particles that has not diffused out of the feldspar; thus a retentivity of one indicates no diffusive loss, while a retentivity asymptoting to zero indicates that steady

state between production and diffusion has occurred. For feldspars exhibiting linear Arrhenius behavior, we assume that the physical grain size defines the diffusion lengthscale of a single diffusion domain and scale diffusivities to a common diffusion lengthscale of 500 μm ; retention curves for these feldspars are shown in [Fig. 9A](#). Having normalized the diffusion lengthscale, we can see in [Fig. 9A](#) that differences in diffusion parameters (E_a and D_0) amongst different feldspars results in significant variability in retentivity. For example, while lunar 76535 anorthite is expected to retain all of its cosmogenic neon over 10 Ma of exposure at 20 °C, Easy Chair Crater anorthoclase would retain <10% given the same exposure history. In cases where we used MDD models to infer neon diffusion parameters, we do not know the diffusion lengthscale of the different domains as this cannot be separated from the preexponential factor D_0 without making additional assumptions. Furthermore, it is likely that the domain size distributions in feldspars exhibiting MDD-like behavior would depend on macroscopic grain size in a way that we cannot quantify. We therefore did the calculations in [Fig. 9B](#) using the spherically equivalent radius of each feldspar crystal analyzed in the stepwise degassing experiment. [Fig. 9B](#) highlights the difference in cosmogenic neon retentivities that would be expected for simple extrapolation of initial linear Arrhenius arrays versus MDD model calculated diffusion parameters in feldspars exhibiting complex Arrhenius behavior. For some feldspars such as Benson Mines orthoclase, the differences are small until very long exposure durations are reached (>1 Ma); for others such as Grass Valley anorthite, the differences become important on much shorter time-scales (>0.01 Ma).

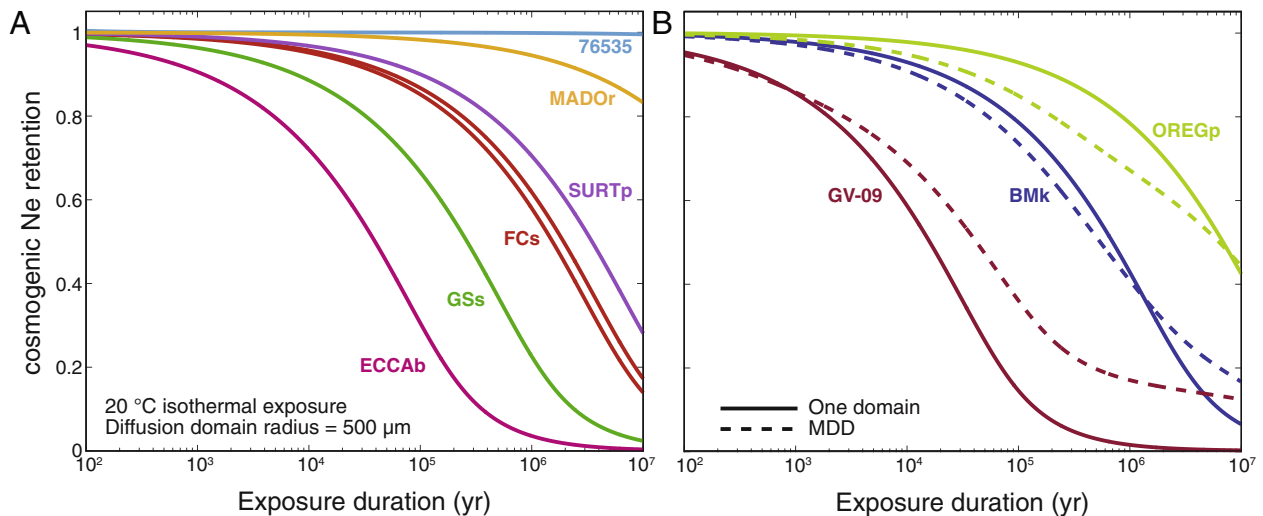


Fig. 9. Demonstration of the variability of neon retentivity in feldspars. Using the neon diffusion parameters reported here and elsewhere ([Gourbet et al., 2012](#); [Garrick-Bethell et al., 2017](#)), we calculate how neon retention evolves as a function of exposure duration assuming a constant exposure temperature of 20 °C after [Wolf et al. \(1998\)](#). In (A), we show neon retention curves for the six feldspars that exhibit relatively simple linear Arrhenius behavior. Simple linear Arrhenius behavior suggests that the physical grain size defines the diffusion lengthscale for these feldspars; therefore we normalized the diffusion lengthscale to a common spherically equivalent radius of 500 μm . In (B), we show neon retention curves for exhibiting complex Arrhenius behavior using diffusion parameters calculated both from the initial linear Arrhenius array (solid curves) observed in stepwise degassing experiments as well as using an MDD model (dashed curves). As discussed in the text, we use the grain size analyzed in the stepwise degassing experiment for these calculations, as there is no straightforward way to normalize the diffusion lengthscale for feldspars exhibiting complex diffusion behavior.

In previous theoretical calculations on the sensitivity of cosmogenic neon-in-feldspar paleothermometry (Tremblay et al., 2014a), we used the diffusion kinetics for Madagascar cryptoperthite reported by Gourbet et al. (2012). However as can be seen in Fig. 9, we predict lower cosmogenic neon retentivity using neon diffusion kinetics from most of the feldspars we examined than when using Madagascar cryptoperthite kinetics. This means that the applicability of cosmogenic noble gas paleothermometry to geologic problems will vary depending on the specific feldspar and surface temperature environment. For example, Kober et al. (2005) measured cosmogenic ^{21}Ne abundances in sanidine from a welded tuff in the Atacama Desert that were indistinguishable from what would be expected given theoretical ^{21}Ne production rates for sanidine and the known exposure duration, suggesting that no diffusive loss of cosmogenic ^{21}Ne occurred. Complete cosmogenic ^{21}Ne retention suggests that the sanidine studied by Kober et al. (2005) is significantly more retentive to neon than the two sanidine samples we conducted stepwise degassing experiments on here, especially given the high amplitude temperature variations and peak temperatures that rocks experience in extreme environments like the Atacama Desert (McKay et al., 2003; McFadden et al., 2005). Similarly, the lunar surface experiences extreme variations in temperature during a lunar day cycle, with peak temperatures in excess of $100\text{ }^\circ\text{C}$ and temperature minima less than $-150\text{ }^\circ\text{C}$ (Keihm and Langseth, 1973). However, because lunar 76535 anorthite is so retentive, Garrick-Bethell et al. (2017) were able to measure cosmogenic neon abundances in multiple anorthite grains and calculate an accurate estimate of the effective lunar surface temperature ($75.5 \pm 4.2\text{ }^\circ\text{C}$) over the 142 Ma exposure history of sample 76535. For any of the diffusion parameters we obtained for the other feldspars, we would predict substantially lower and incorrect effect lunar surface temperatures.

5. CONCLUSIONS

We present stepwise neon degassing experiments on feldspars of various compositions and geologic origins. This suite of experiments reveals that neon diffusion behavior and kinetics vary significantly amongst different feldspars. Comparison with argon stepwise degassing experiments on the same feldspars provides insight into the source of complex noble gas diffusion behavior. For some feldspars, the absence of nonlinear Arrhenius behavior in neon experiments conducted at lower temperatures suggests that the nonlinear behavior observed in argon experiments resulted from temperature-dependent structural transformations. For other feldspars, nonlinear Arrhenius behavior observed in both neon and argon experiments suggests that some sample-specific material property is contributing to complex diffusion behavior. When extrapolated down to planetary surface temperatures, the set of available neon diffusion kinetics predicts a wide range of temperatures and exposure durations over which cosmogenic noble gas paleothermometry may be applicable. This wide range indicates that (1) sample specific diffusion kinetics will be necessary for quantitative applications, and (2) the temperature

sensitivity of cosmogenic noble gas paleothermometry will depend greatly on a combination of the specific feldspar and surface thermal environment of interest.

ACKNOWLEDGEMENTS

We thank R. Wenk and D. Mark for providing samples. We also thank N. Fylstra, T. Becker, and J. Maisano for analytical assistance. AE Greg Herzog and three reviewers provided constructive feedback that strengthened this work. We acknowledge support from the NSF Petrology and Geochemistry Program (EAR-1322086), the UC Berkeley Larsen Grant, and the Ann and Gordon Getty Foundation. MMT was supported by an NSF Graduate Research Fellowship.

APPENDIX A. SUPPLEMENTARY DATA

Supplementary data associated with this article can be found, in the online version, at <http://dx.doi.org/10.1016/j.gca.2017.02.013>.

REFERENCES

- Bachmann O., Dungan M. A. and Lipman P. W. (2002) The Fish Canyon Magma Body, San Juan Volcanic Field, Colorado: rejuvenation and Eruption of an Upper-Crustal Batholith. *J. Petrol.* **43**, 1469–1503.
- Balco G. and Shuster D. L. (2009) Production rate of cosmogenic ^{21}Ne in quartz estimated from ^{10}Be , ^{26}Al , and ^{21}Ne concentrations in slowly eroding Antarctic bedrock surfaces. *Earth Planet. Sci. Lett.* **281**, 48–58.
- Berger G. W. and York D. (1981) Geothermometry from $^{40}\text{Ar}/^{39}\text{Ar}$ dating experiments. *Geochim. Cosmochim. Acta* **45**, 795–811.
- Brown W. L., Openshaw R. E., McMillan P. F. and Henderson M. B. (1984) A review of the expansion behavior of alkali feldspars: coupled variations in cell parameters and possible phase transitions. *Am. Mineral.* **69**, 1058–1071.
- Cassata W. S. and Renne P. R. (2013) Systematic variations of argon diffusion in feldspars and implications for thermochronometry. *Geochim. Cosmochim. Acta* **112**, 251–287.
- Cassata W. S., Shuster D. L., Renne P. R. and Weiss B. P. (2010) Evidence for shock heating and constraints on Martian surface temperatures revealed by $^{40}\text{Ar}/^{39}\text{Ar}$ thermochronometry of Martian meteorites. *Geochim. Cosmochim. Acta* **74**, 6900–6920.
- Crank J. (1975) *The Mathematics of Diffusion*. Oxford University Press, London.
- Evernden J. F., Curtis G. H., Kistler R. W. and Obradovich J. D. (1960) Argon diffusion in glauconite, microcline, sanidine, leucite and phlogopite. *Am. J. Sci.* **258**, 583–604.
- Fechtig H. and Kalbitzer S. (1966) The Diffusion of Argon in Potassium-Bearing Solids. In Potassium Argon Dating pp. 68–107.
- Fechtig H., Gentner W. and Zähringer J. (1960) Argonbestimmungen an Kaliummineralien—VII Diffusionsverluste von Argon in Mineralien und ihre Auswirkung auf die Kalium-Argon-Altersbestimmung. *Geochim. Cosmochim. Acta* **19**, 70–79.
- Jr Foit F. F. and Peacor D. R. (1973) The Anorthite Crystal Structure at 410 and 830 & #xB0;C. *Am. Mineral.* **58**, 665–675.
- Foland K. A. and Xu Y. (1990) Diffusion of ^{40}Ar and ^{39}Ar in irradiated orthoclase. *Geochim. Cosmochim. Acta* **54**, 3147–3158.

- Garrick-Bethell I., Weiss B. P., Shuster D. L., Tikoo S. M. and Tremblay M. M. (2017) Further evidence for early lunar magnetism from troctolite 76535. *J. Geophys. Res.: Planets*.
- Gautheron C. and Tassan-Got L. (2010) A Monte Carlo approach to diffusion applied to noble gas/helium thermochronology. *Chem. Geol.* **273**, 212–224.
- Gerling E. K., Leviski L. K. and Morozova I. M. (1963) On the diffusion of radiogenic argon from minerals. *Geokhimiya* **6**. Available at: <http://www.osti.gov/scitech/biblio/4712579>.
- Gourbet L., Shuster D. L., Balco G., Cassata W. S., Renne P. R. and Rood D. (2012) Neon diffusion kinetics in olivine, pyroxene and feldspar: Retentivity of cosmogenic and nucleogenic neon. *Geochim. Cosmochim. Acta* **86**, 21–36.
- Harrison T. M. and McDougall I. (1982) The thermal significance of potassium feldspar K-Ar ages inferred from $^{40}\text{Ar}/^{39}\text{Ar}$ age spectrum results. *Geochim. Cosmochim. Acta* **46**, 1811–1820.
- Harrison T. M., Lovera O. M. and Matthew T. H. (1991) $^{40}\text{Ar}/^{39}\text{Ar}$ results for alkali feldspars containing diffusion domains with differing activation energy. *Geochim. Cosmochim. Acta* **55**, 1435–1448.
- Herman F., Seward D., Valla P. G., Carter A., Kohn B., Willett S. D. and Ehlers T. A. (2013) Worldwide acceleration of mountain erosion under a cooling climate. *Nature* **504**, 423–426.
- Hodges K. V., Ruhl K. W., Wobus C. W. and Pringle M. S. (2005) $^{40}\text{Ar}/^{39}\text{Ar}$ thermochronology of detrital minerals. *Rev. Mineral. Geochem.* **58**, 239–257.
- Hovis G. L., Brennan S., Keohane M. and Crelling J. (1999) High-temperature X-ray investigation of sanidine – analbite crystalline solutions: thermal expansion, phase transitions, and volumes of mixing. *Canadian Mineral.* **37**, 701–709.
- Hovis G. L., Medford A., Conlon M., Tether A. and Romanoski A. (2010) Principles of thermal expansion in the feldspar system. *Am. Mineral.* **95**, 1060–1068.
- Huber C., Cassata W. S. and Renne P. R. (2011) A lattice Boltzmann model for noble gas diffusion in solids: The importance of domain shape and diffusive anisotropy and implications for thermochronometry. *Geochim. Cosmochim. Acta* **75**, 2170–2186.
- Jourdan F., Moynier F., Koeberl C. and Eroglu S. (2011) $^{40}\text{Ar}/^{39}\text{Ar}$ age of the Lunar crater and consequence for the geochronology of planetary impacts. *Geology* **39**, 671–674.
- Keihm S. J. and Langseth M. G. Jr (1973) Surface brightness temperatures at the Apollo 17 heat flow site: Thermal conductivity of the upper 15 cm of regolith. In Lunar and Planetary Science Conference Proceedings adsabs.harvard.edu. p. 2503.
- Ketchum R. A. (2005) Computational methods for quantitative analysis of three-dimensional features in geological specimens. *Geosphere* **1**, 32–41.
- Ketchum R. A. and Carlson W. D. (2001) Acquisition, optimization and interpretation of X-ray computed tomographic imagery: applications to the geosciences. *Comput. Geosci.* **27**, 381–400.
- Kober F., Ivy-Ochs S., Leya I., Baur H., Magna T., Wieler R. and Kubik P. W. (2005) In situ cosmogenic ^{10}Be and ^{21}Ne in sanidine and in situ cosmogenic ^3He in Fe–Ti-oxide minerals. *Earth Planet. Sci. Lett.* **236**, 404–418.
- Koning A. J., Rochman D., Kopecky J., Ch. Sublet J., Bauge E., Hilaire S., Romain P., Morillon B., Duarte H., van der Marck S., Pomp S., Sjostrand H., Forrest R., Henriksson H., Cabellos O., Goriely S., Leppanen J., Leeb H., Plompen A. and Mills R. (2015) TENDL-2015. *TENDL-2015: TALYS-based evaluated nuclear data library*. Available at: https://tendl.web.psi.ch/tendl_2015/tendl2015.html.
- Lovera O. M. and Richter F. M. (1989) The $^{40}\text{Ar}/^{39}\text{Ar}$ thermochronometry for slowly cooled samples. *J. Geophys. Res.* **94**, 17–917.
- Lovera O. M., Richter F. M. and Harrison T. M. (1991) Diffusion domains determined by ^{39}Ar released during step heating. *J. Geophys. Res.* **96**, 2057–2069.
- Lovera O. M., Heizler M. T. and Harrison T. M. (1993) Argon diffusion domains in K-feldspar II: kinetic properties of MH-10. *Contrib. Mineral. Petrol.* **113**, 381–393.
- Lovera O. M., Grove M., Harrison T. M. and Mahon K. I. (1997) Systematic analysis of K-feldspar $^{40}\text{Ar}/^{39}\text{Ar}$ step heating results: I. Significance of activation energy determinations. *Geochim. Cosmochim. Acta* **61**, 3171–3192.
- Lovera O. M., Grove M. and Harrison T. M. (2002) Systematic analysis of K-feldspar $^{40}\text{Ar}/^{39}\text{Ar}$ step heating results II: relevance of laboratory argon diffusion properties to nature. *Geochim. Cosmochim. Acta* **66**, 1237–1255.
- Lovera O. M., Harrison T. M. and Boehnke P. (2015) Comment on “Systematic variations of argon diffusion in feldspars and implications for thermochronometry” by Cassata and Renne. *Geochim. Cosmochim. Acta* **151**, 168–171.
- McFadden L. D., Eppes M. C., Gillespie A. R. and Hallet B. (2005) Physical weathering in arid landscapes due to diurnal variation in the direction of solar heating. *GSA Bull.* **117**, 161–173.
- McKay C. P., Friedmann E. I., Gómez-Silva B., Cáceres-Villanueva L., Andersen D. T. and Landheim R. (2003) Temperature and moisture conditions for life in the extreme arid region of the Atacama desert: four years of observations including the El Niño of 1997–1998. *Astrobiology* **3**, 393–406.
- McLaren A. C. and Marshall D. B. (1974) Transmission electron microscope study of the domain structures associated with the b-, c-, d-, e- and f-reflections in plagioclase feldspars. *Contrib. Mineral. Petrol.* **44**, 237–249.
- McLaren S., Dunlap W. J. and Powell R. (2007) Understanding K-feldspar $^{40}\text{Ar}/^{39}\text{Ar}$ data: reconciling models, methods and microtextures. *J. Geol. Soc. London* **164**, 941–944.
- Meesters A. G. C. A. and Dunai T. J. (2002) Solving the production–diffusion equation for finite diffusion domains of various shapes: Part I. Implications for low-temperature (U–Th)/He thermochronology. *Chem. Geol.* **186**, 333–344.
- Megaw H. D., Kempster C. J. E. and Radoslovich E. W. (1962) The structure of anorthite, $\text{CaAl}_2\text{Si}_2\text{O}_8$ II. Description and discussion. *Acta Crystallogr.* **15**, 1017–1035.
- Min K., Reiners P. W., Nicolescu S. and Greenwood J. P. (2004) Age and temperature of shock metamorphism of Martian meteorite Los Angeles from (U–Th)/He thermochronometry. *Geology* **32**, 677.
- Parsons I. (2010) Feldspars defined and described: a pair of posters published by the Mineralogical Society. Sources and supporting information. *Mineral. Mag.* **74**, 529–551.
- Parsons I., Brown W. L. and Smith J. V. (1999) $^{40}\text{Ar}/^{39}\text{Ar}$ thermochronology using alkali feldspars: real thermal history or mathematical mirage of microtexture? *Contrib. Mineral. Petrol.* **136**, 92–110.
- Rainey C. S. and Wenk H.-R. (1978) Intensity differences of subsidiary reflections in calcic plagioclase. *Am. Mineral.* **63**, 124–131.
- Reynolds J. H. (1957) Comparative study of argon content and argon diffusion in mica and feldspar. *Geochim. Cosmochim. Acta* **12**, 177–184.
- Richter F. M., Lovera O. M., Harrison T. M. and Copeland P. (1991) Tibetan tectonics from $^{40}\text{Ar}/^{39}\text{Ar}$ analysis of a single K-feldspar sample. *Earth Planet. Sci. Lett.* **105**, 266–278.
- Schairer J. F. (1950) The Alkali-Feldspar join in the system $\text{NaAlSi}_3\text{O}_8$ – KAlSi_3O_8 – SiO_2 . *J. Geol.* **58**, 512–517.
- Shuster D. L. and Cassata W. S. (2015) Paleotemperatures at the lunar surfaces from open system behavior of cosmogenic ^{38}Ar and radiogenic ^{40}Ar . *Geochim. Cosmochim. Acta* **155**, 154–171.

- Shuster D. L. and Farley K. A. (2005a) $^4\text{He}/^3\text{He}$ thermochronometry: theory, practice, and potential complications. *Rev. Mineral. Geochem.* **58**, 181–203.
- Shuster D. L. and Farley K. A. (2005b) Diffusion kinetics of proton-induced ^{21}Ne , ^3He , and ^4He in quartz. *Geochim. Cosmochim. Acta* **69**, 2349–2359.
- Shuster D. L. and Farley K. A. (2009) The influence of artificial radiation damage and thermal annealing on helium diffusion kinetics in apatite. *Geochim. Cosmochim. Acta* **73**, 183–196.
- Shuster D. L., Farley K. A., Sistierson J. M. and Burnett D. S. (2004) Quantifying the diffusion kinetics and spatial distributions of radiogenic ^4He in minerals containing proton-induced ^3He . *Earth Planet. Sci. Lett.* **217**, 19–32.
- Shuster D. L., Balco G., Cassata W. S., Fernandes V. A., Garrick-Bethell I. and Weiss B. P. (2010) A record of impacts preserved in the lunar regolith. *Earth Planet. Sci. Lett.* **290**, 155–165.
- Smith J. V. and Ribbe P. H. (1969) Atomic movements in plagioclase feldspars: Kinetic interpretation. *Contrib. Mineral. Petrol.* **21**, 157–202.
- Tremblay M. M., Shuster D. L. and Balco G. (2014a) Cosmogenic noble gas paleothermometry. *Earth Planet. Sci. Lett.* **400**, 195–205.
- Tremblay M. M., Shuster D. L. and Balco G. (2014b) Diffusion kinetics of ^3He and ^{21}Ne in quartz and implications for cosmogenic noble gas paleothermometry. *Geochim. Cosmochim. Acta* **142**, 186–204.
- Tribaudino M., Angel R. J., Cámara F., Nestola F., Pasqual D. and Margiolaki I. (2010) Thermal expansion of plagioclase feldspars. *Contrib. Mineral. Petrol.* **160**, 899–908.
- Turner G. (1971) ^{40}Ar - ^{39}Ar ages from the lunar maria. *Earth Planet. Sci. Lett.* **11**, 169–191.
- Van Tendeloo G., Ghose S. and Amelinckx S. (1989) A dynamical model for the P1–I1 phase transition in anorthite, $\text{CaAl}_2\text{Si}_2\text{O}_8$. *Phys. Chem. Miner.* **16**, 311–319.
- Villa I. M. (2006) From nanometer to megameter: Isotopes, atomic-scale processes, and continent-scale tectonic models. *Lithos* **87**, 155–173.
- Villa I. M. and Hanchar J. M. (2013) K-feldspar hydrochronology. *Geochim. Cosmochim. Acta* **101**, 24–33.
- Wolf R. A., Farley K. A. and Kass D. M. (1998) Modeling of the temperature sensitivity of the apatite (U–Th)/He thermochronometer. *Chem. Geol.* **148**, 105–114.

Associate editor: Gregory F. Herzog